Polymer 50 (2009) 3797–3809

Contents lists available at ScienceDirect

Polymer

journal homepage: www.elsevier.com/locate/polymer

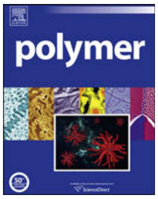

Processing-property relationships of polycarbonate/graphene composites

Hyunwoo Kim, Christopher W. Macosko*

Department of Chemical Engineering and Materials Science, University of Minnesota, 421 Washington Ave. SE, Minneapolis, MN 55455-0132, USA

ARTICLE INFO

Article history:
Received 10 January 2009
Received in revised form
16 May 2009
Accepted 19 May 2009
Available online 27 May 2009

Keywords:
Layered graphite nanocomposites
Melt compounding
Flow orientation

ABSTRACT

Polycarbonate composites reinforced with graphite and functionalized graphene sheets (FGS) were produced using melt compounding. Composite samples with different degrees of graphite orientation were processed via injection, compression molding and long-term annealing. Electron microscopy and X-ray scattering revealed that FGS was nearly exfoliated. However, graphite remained multi-layer even after melt processing. Flow induced orientation of graphite was observed from both injection and compression molded samples. Graphite particles in samples after long-term annealing exhibited more random orientation. Composites with the exfoliated FGS required a smaller amount of reinforcement for rigidity and connectivity percolation, as determined by melt rheology and electrical conductivity measurements. FGS also showed better performance in suppressing gas permeability of polycarbonate. However, improvements by FGS dispersion in tensile modulus and dimensional stability were not as significant. This may be due to defects in the sheet structure formed during oxidation and pyrolysis used to exfoliate.

1. Introduction

Graphite has attracted large interest as a reinforcement for polymers because of its potential to modify their mechanical and electrical properties [1,2]. In-plane Young's modulus and electrical conductivity of graphite are as high as those of carbon nanotubes (CNT) ($E \sim 1$ TPa, $\sigma \sim 10^6$ (ohm cm)$^{-1}$) [3–5]. If graphite can be exfoliated, it can improve the properties at relatively smaller loading compared with conventional carbon fillers such as carbon black and fibers [2]. Another advantage over other carbon reinforcements is that these 2-dimensional nano-lamellae can reduce gas permeation of polymeric membranes significantly [6–8]. These property gains by graphite addition can be maximized when the morphology of graphite composites is tailored such that dispersed particles have the highest aspect ratio and their orientation is controlled appropriately throughout the matrix.

However, control over dispersion and orientation of graphite is not attained easily. Strong molecular binding between graphene stacks and low solubility in organic solvents and polymers prevent the use of conventional composite manufacturing strategies: solution blending and melt intercalation. Higher surface area can be obtained by treating graphite intercalation compounds with heat or microwaves to separate layers before incorporation into polymers [9–12]. However, the resulting layers are still far thicker ($\sim$100 nm) than single graphene sheets (0.34 nm) [13]. It was reported recently that rapid pyrolysis of graphite oxide leads to complete exfoliation of the carbon sheets [14,15]. Epoxide and hydroxyl groups on the graphite oxide surface decompose by fast heating up to $\sim$1050 °C under argon with the conversion into CO_2 which pressurizes and splits apart the graphene layers [16]. Oxidation and thermal exfoliation result in permanent deformation of sheets into a wrinkled structure by transformation of sp^2-hybridized carbons into sp^3 hybridization, preventing restacking of layers [17]. Unlike graphite oxide which lacks electrical conductivity, thermally exfoliated graphite oxide has high electrical conductivity, comparable to that of untreated graphite [14] and its high aspect ratio implies applications to gas diffusion barrier membranes [7,8].

We chose this thermally exfoliated graphite oxide (functionalized graphene sheets, FGS) to reinforce poly(ethylene-2,6-naphthalate) (PEN), a high temperature engineering polyester. We found that FGS improved electrical conductivity, melt viscoelasticity and gas barrier properties of PEN at significantly smaller loading than typical graphite [7]. However, despite its high aspect ratio, FGS was not as efficient in enhancing modulus and dimensional stability of PEN. We speculated that structural defects, such as sheet wrinkling, formed during oxidation and high temperature FGS synthesis reduced the effective stiffness of the graphene sheets.

Orientation of high aspect ratio particles also plays an important role in composite properties. In-plane alignment of graphite

---

* Corresponding author. Tel.: +1 612 625 0092; fax: +1 612 626 1686.
E-mail addresses: kim@cems.umn.edu (H. Kim), macosko@umn.edu (C.W. Macosko).

0032-3861/$ – see front matter © 2009 Elsevier Ltd. All rights reserved.
doi:10.1016/j.polymer.2009.05.038

ellipsoids are favored for improving mechanical and barrier properties in selected directions. Composite stiffness will be highest in a direction along which layers are oriented, whereas gas permeation will be lowest perpendicular to the orientation [18,19]. Property improvements that require rigidity and connectivity percolation of filler networks generally benefit from the random orientation [20,21]. Shear orientation of CNT or clay/polymer hybrid melts can change their viscoelastic behavior from solid to liquid-like [20,22]. Electrical conduction of anisotropic particle networks decreases as their orientation becomes more anisotropic [21,23–25]. Orientation eliminates contacts between neighboring particles destroying the continuous network needed to resist deformation or transfer charge carriers.

In this article, processing, morphology and properties of polycarbonate (PC) reinforced with graphite are reported. PC is one of the most important commodity polymers due to good mechanical and thermal properties, impact resistance and optical transparency. Its amorphous nature allows us to circumvent complexities of interpreting property changes associated with crystallization versus graphite addition. Its high melt stability prevents thermal degradation during prolonged rheological measurements. Pötschke and coworkers reported that electrical conductivity and melt viscoelasticity of PC could be modified significantly with small incorporation of carbon nanotubes (1–2 wt%) [26,27]. Similar benefits are also expected from graphitic nano-platelets. We chose two graphite reinforcements that can lead to different states of dispersion: FGS and un-exfoliated flake graphite. After blending PC with graphite and FGS using melt compounding, orientation of graphite plates in samples was controlled via different types of post-processing: long-term annealing, compression and injection molding. Dispersion and orientation of graphite nano-fillers were characterized with electron microscopy and X-ray scattering. Their effects on melt viscoelasticity and electrical conductivity are also presented as well as tensile and bending moduli, thermal expansion and gas permeability.

2. Experimental

2.1. Materials

The matrix material used in this study was Calibre 201-22 PC resin from Dow Chemical. 201-22 is an injection molding grade with a melt flow index of 22 g/10 min at 300 °C and its solid density is 1.2 g/cm^3 [28]. Polystyrene-calibrated number (M_n) and weight (M_w) averaged molecular weight of Calibre 202-22 are 27.1 and 50.4 kg/mol respectively, as determined by size exclusion chromatography (SEC) in chloroform. Pellets were dried in an oven at 90 °C at least for 24 h before melt processing. Flake graphite (surface enhanced, grade # 3775) was purchased from Asbury Carbons [29]. Specific surface area of graphite measured by the Brunauer, Emmet and Teller (BET) [30] N_2 adsorption (Autosorb-1, Quantachrome Instruments) was 29 m^2/g, which is close to 24 m^2/g provided by the supplier and higher than that of typical natural graphite [31]. FGS, a thermally treated graphite oxide was generously provided by Vorbeck materials [32]. Its BET surface area, ~800 m^2/g is substantially greater than that of graphite and within the range of 700–1500 m^2/g, an estimate by Schniepp and coworkers [14].

Melt density of PC, ~1.1 g/cm^3 was calculated based on Bohlen and Kirchheim's volumetric expansion coefficient data [33]. Density of graphite, 2.28 g/cm^3 was estimated from unit cell dimensions of perfectly crystalline graphite [34]; FGS is assumed to have the same density. Our previous observation [7] using atomic force microscopy (AFM), Raman spectroscopy and X-ray photoelectron spectroscopy (XPS) agreed with the results reported by Schniepp et al. [14,35]: FGS is in a nearly fully exfoliated state with structural distortions (e.g. buckling) from oxidation and superheating.

2.2. Processing

Graphite and FGS were incorporated into PC by melt blending, using a DACA microcompounder, a small scale, conical, twin screw extruder with a recirculation channel [36]. PC blends containing 0, 1, 3, 5, 6, 7, 8.5, 10 and 12 wt% of graphite and 0.25, 0.5, 0.75, 1.0, 1.25, 1.5, 2.0, 2.5 and 3.0 wt% of FGS were prepared with the DACA extruder at 250 °C for 8 min under N_2 purge. Screw speed was 200 rpm. Due to the limited amount of FGS available to us, large scale twin screw compounding was carried out only with graphite. 200–250 g of PC pellets were physically mixed with 0, 1, 5 and 10 wt% of graphite by shaking them together in a plastic container. Graphite was added in ~1% excess by weight than calculated amount to compensate for losses in the feed hopper. They were loaded onto the hopper of a 16 mm co-rotating PRISM TSE 16TC twin screw extruder. Screws were configured with three kneading blocks and one back-mixing block separated by forward conveying zones [37]. Temperature was maintained at 250 °C in the mixing zones and the exit die, and 230 °C in the feeding zone. Screw speed was kept around 110 rpm in order not to exceed 75–90% of maximum allowed torque level (20 N m). Extrudates were cooled in a water bath and dried by hot air before pelletized. SEC confirmed matrix molecular weights changed less than 2% during melt processing.

After melt processing, extruded materials were stored at 90 °C to prevent moisture inclusion. They were then molded into three different geometries (see Fig. 1) in order to study the influence of processing on graphite orientation and composite properties. Sample geometries were 150–200 μm thick films (F samples), rectangular bars (10 cm × 3.25 mm × 12.8 mm, B samples) and 1 mm thick, 25 mm diameter disks (D samples). F samples were formed by placing DACA extrudates between Teflon coated aluminum foil in a hydraulic hot press at 260 °C and applying pressure (100 kPa) for 2 min. B samples were produced by ram injection molding (Morgan Press, Morgan Industries). 100 g of twin screw extruded pellets were fed into the injection molder. The barrel, nozzle and mold temperature were set to 265, 275 and 135 °C, respectively. For samples with

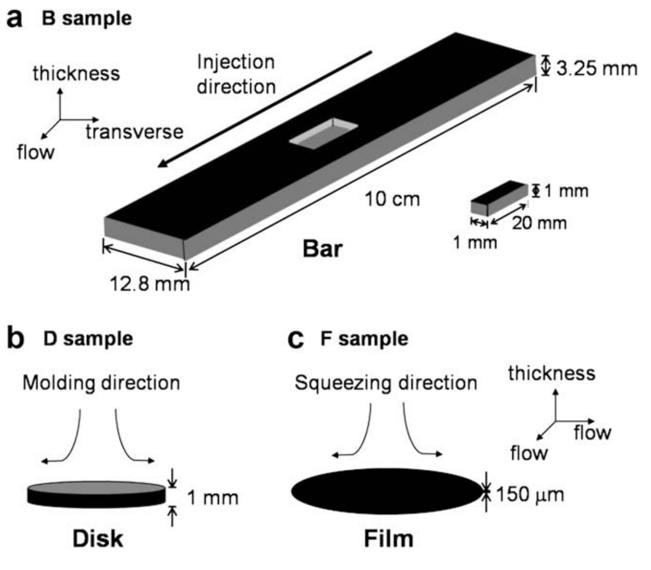

Fig. 1. Sample geometries and definitions for 3 orthogonal directions for (a) B, (b) D and (c) F samples.

higher graphite concentration, higher processing temperature was required (for instance, 280, 290 and 145 °C for 10 wt% graphite samples) to facilitate mold filling. D samples were compression molded from DACA extrudates using disk-shaped molds and the hot press. After melting at 260–270 °C, they were pressed under 50 kPa pressure in the 1 mm thick molds for 2 min. D samples were annealed at 265 °C for 30 min. In order to reduce effects from orientation of graphite and FGS during compression molding, some disks were annealed longer at 230–250 °C for 24–48 h under N_2 atmosphere using the environmental chamber of the rotational rheometer (ARES, TA Instruments).

2.3. Direct characterization of dispersion and orientation

Dispersion of graphitic additives in PC matrix was characterized with transmission electron microscopy (TEM). PC composites containing 6 wt% graphite and 3 wt% FGS as DACA extruded were microtomed (Reichert Ultracut) at room temperature into 70–90 nm thick slices with a diamond knife and placed onto 400-mesh Cu grids. Micrographs were collected using a JEOL 1210 electron microscope at the accelerating voltage of 120 kV.

Wide angle X-ray scattering was conducted with a micro-diffractometer (Bruker-AXS) and CuKα radiation (45 kV and 40 mA). 1 mm × 1 mm × 20 mm bar-shaped specimens (B and D samples) and 1 mm wide, 20 mm long films (F samples) were cut from the composite samples, and mounted in a 1/4 circle Eulerian sample holder. Due to the spatial variations of graphite orientation in the B samples, 1 mm thick bars were obtained from a fixed location, an outer skin at the center of the largest face (10 cm × 12.8 mm) as illustrated in Fig. 1(a). X-rays were directed in 3 different directions (flow, transverse and thickness) for B samples to probe graphite orientation. For F and D samples, only flow and thickness directions were used due to their transverse isotropy. All azimuthal scans in Figs. 4 and 5 are shown after background subtraction using scattered intensity from neat PC samples with the same geometry.

2.4. Melt rheology

Viscoelastic properties of the composite melts were studied with the ARES rheometer. 0.6–0.7 g of DACA extrudates were dried at 90 °C and placed on 25 mm parallel plates at 230 °C. After about 5 min heating, the upper plate was slowly lowered at 0.002 mm/s until the plates were ~1 mm apart. A "dynamic strain sweep" at frequency ω of 1 rad/s was used to find the critical strain γ_{crit} for linear viscoelasticity; γ_{crit} was the strain at which G' drops to 90% of its limiting low strain value. Then, "dynamic time sweep" was run for 10,000–12,000 s at 0.1 rad/s to monitor changes in dynamic storage modulus G' and loss modulus G'' versus time. Test strain was set at less than 10% of the critical strain before annealing to avoid shear induced orientation of graphite layers. After the time sweep, γ_{crit} after annealing was evaluated using a second strain sweep. A time sweep at 0.1 rad/s for 10,000–12,000 s followed to monitor the recovery of the graphite network disrupted by the large amplitude straining. Finally, a dynamic frequency sweep was conducted from 100 rad/s to 0.01 rad/s at $\gamma < \gamma_{crit}$. Occasionally, the length of the time sweep was doubled ($t = 20{,}000$–$24{,}000$ s) or extended to even longer to examine the effect of prolonged annealing on the structural evolution of the graphite networks. Results were reproduced in tests repeated with varying the gap between parallel plates, which confirms ~1 mm gap was large enough to ensure the sample uniformity. Note that the longest dimensions of particles (graphite: 100–1000 nm and FGS: 50–400 nm [7]) are significantly smaller than 1 mm.

2.5. Property measurements

Surface resistance was measured using an 11-probe DC resistance meter (Prostat-801). Sample surfaces were polished ~10 μm deep with fine sandpaper (P600 grade) to reduce contact resistance. Resistance was obtained from 3 to 4 different areas near the center of as-squeezed F samples and annealed D samples and their geometric average values are reported. For B samples, the probe was placed at the center of the 10 cm × 12.8 mm plane, the same location where X-ray scattering specimens were obtained. Measurements were made on both unpolished and polished sides of B samples to find effects of polishing on the conductivity measurements.

Dynamic tensile and bending moduli of composite samples were measured with a Rheometrics Solids Analyzer II (RSA II). For tests in tensile mode, F samples were used due to their small sample thickness and high in-plane particle orientation. 5 mm wide and 30 mm long strips were cut from the films and clamped between film fixtures of the RSA II. Dynamic strain sweep tests at 1 rad/s were started from 0.002% strain under a static pretension of ~10 N to prevent sample buckling. For three point bending tests, we used the injection molded bars (B samples). They were placed on two outer points which are 4.8 cm apart and deformed by the third central point from the opposite side. Dynamic strain sweeps from 0.002% were conducted under a static bending force of 20 N. For thermal expansion measurements, dimensional changes of F samples were traced while sequentially changing temperature from 65 to 50, 35 and 25 °C in the N_2 convection chamber of RSA II. Prior to the measurements, specimens were dried at 65 °C with N_2 dry purge for 3.5 h to exclude effects from hygroscopic expansion.

N_2 and He permeation coefficients through the film (F) samples were determined at 35 °C based on a constant volume-variable pressure method using a home-built gas permeation apparatus [38,39]. N_2 or He was introduced in one side of a 42 mm diameter composite disk at 1 atm; the opposite side was evacuated overnight. Permeability was calculated from the pressure change over time in the downstream compartment, pressure difference across the membrane (1 atm), and the sample thickness and area.

3. Results and discussion

3.1. TEM analysis

Fig. 2 shows TEM micrographs of 6 wt% graphite/PC, and 3 wt% FGS/PC composites. In Fig. 2(a) and (b), only one or two graphite platelets (~40 nm thick) oriented perpendicular to the sample surface are visible over the entire imaging area (2 μm × 2 μm). During melt blending, there was no noticeable change in particle thickness from the average thickness of unmixed particles estimated from the BET surface area assuming disk-like particles (~30 nm) or from the thickness measured by AFM analysis (~37 nm) [7]. This indicates only breaking up of weakly aggregated graphite platelets took place during melt compounding. The multiple layer structure of graphite becomes more evident from the face-on view of a graphite particle in Fig. 2(c). The image is very dark indicating many graphene layers. In contrast, in the micrographs of FGS/PC, such dark images are never observed. Also, much thinner FGS layers (1–4 nm thick) are more evenly distributed despite their lower concentration (Fig. 2(d)). Considering the average thickness of fully exfoliated FGS layers, ~1.8 nm measured by Schniepp et al. [14], or ~1.1 nm estimated from the BET surface area ~800 m^2/g of as-received FGS particles, this range of thickness corresponds to a single or a few stacked sheets. It is noteworthy that edges of FGS sheets in Fig. 2(d) are aligned in one direction, which signifies a flow induced orientation during extrusion process. Higher magnification imaging reveals wrinkling of FGS

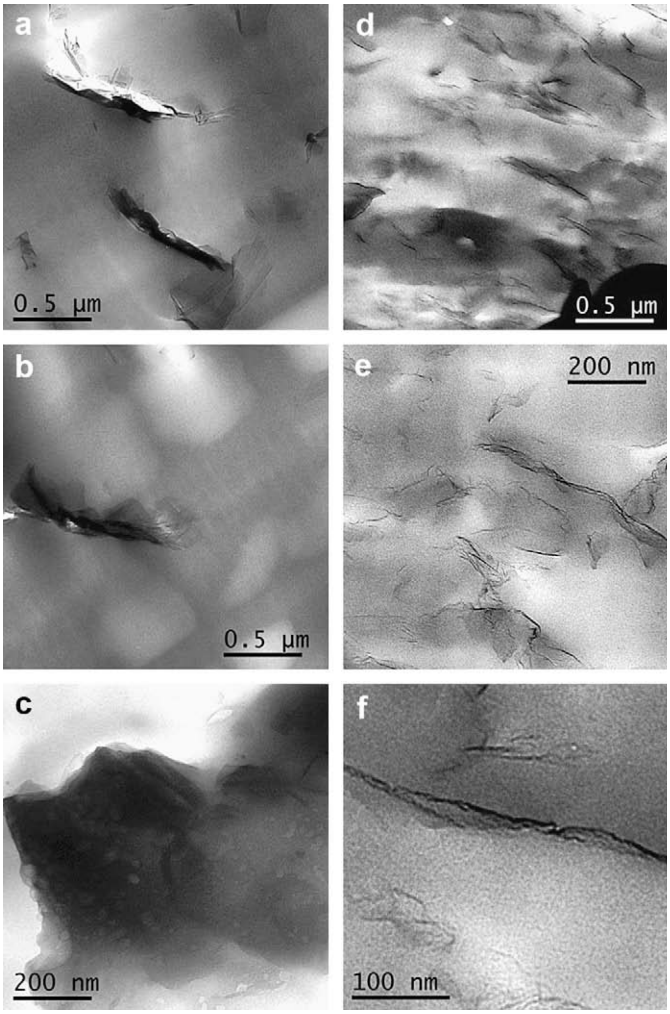

Fig. 2. TEM micrographs of PC composites microtomed from microcompounder extrudates. 6 wt% graphite: (a) and (b) particles oriented edge on, and (c) particles face on. 3 wt% FGS: (d), (e) and (f).

layers (Fig. 2(f)). As suggested by Raman spectroscopy and XPS [7,35], planar graphene carbons (sp^2-hybridized) were transformed into out of plane ones (sp^3-hybridized) by surface oxygen functionalities (C–O and C–O–C), resulting in buckling of the sheets.

3.2. X-ray scattering

Dispersion and orientation of graphite in PC composites were analyzed from 2-dimensional X-ray scattering. When the intensity is integrated as a function of scattering angle 2θ, a sharp reflection is present at $2\theta = 26.4°$ for graphite composites which corresponds to the interlayer spacing of un-intercalated graphite ($d = 0.34$ nm) while this peak is absent for FGS composites and neat PC (Fig. 3). This corroborates the TEM results: after melt dispersion in PC, graphite remains highly layered while FGS is highly exfoliated. Regardless of their previous processing history, every graphite sample exhibited this reflection in its X-ray scattering pattern. There was also a variation in intensity depending on the azimuthal angle ϕ in the 2-D scattering profile along the semicircle of $2\theta = 26.4°$. Azimuthal scans integrated over $2\theta = 26.0–26.8°$ of 10 wt% graphite B sample are shown in Fig. 4(a). In the scans of the flow and the transverse directions, scattering from graphite interlayer is strong and intensity is concentrated at $\phi = -90°$, indicating graphite platelets near the sample skin adopt in-plane orientation parallel to the surface (co-planar with transverse and flow direction). For D and F samples, X-ray was only directed along only 2 axes since these samples are transversely isotropic. Similar to the

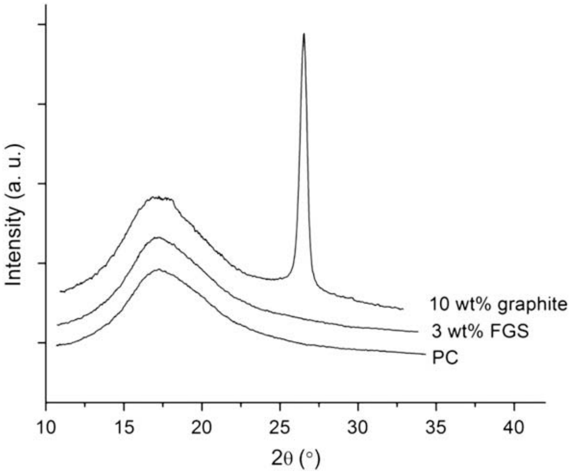

Fig. 3. Scattering intensity profile of neat PC and 3 wt% FGS/PC as DACA extruded, and 10 wt% graphite/PC B sample from X-ray incident in transverse direction. Curves are offset vertically for clarity.

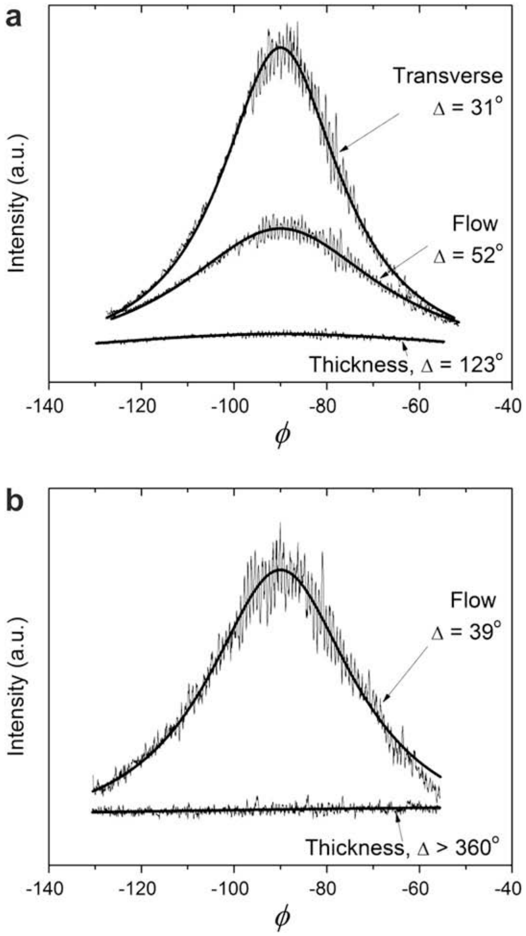

Fig. 4. Azimuthal X-ray scattering scans (scattered curves) at $2\theta = 26.4° \pm 0.4$ of (a) skin parts of 10 wt% graphite B samples and (b) 7 wt% graphite F samples with X-ray directions in flow, transverse and thickness direction. Fits (smooth curves) with the Lorentzian distribution function (equation (1)) are also shown.

injection molded B samples, intensity is concentrated at $\phi = -90^\circ$ from the X-ray scan in flow direction, implying graphite alignment parallel to the sample surface (Fig. 4(b) and Fig. 5). Extent of alignment of anisotropic particles can be quantified by fitting scattering intensity distribution $I(\phi)$ with the Lorentzian function [20,24,40]

$$I(\phi) = \frac{1}{\pi}\frac{\Delta/2}{(\phi-\phi_0)^2+(\Delta/2)^2} \tag{1}$$

where ϕ_0 and Δ are the center and a full width at half maximum (FWHM) of the distribution, respectively. As shown in Fig. 4, FWHM, Δ of azimuthal scans in flow or transverse direction are all smaller than 90°. Shear and extensional flow of PC/graphite melt during injection and compression molding is expected to orient the platelets.

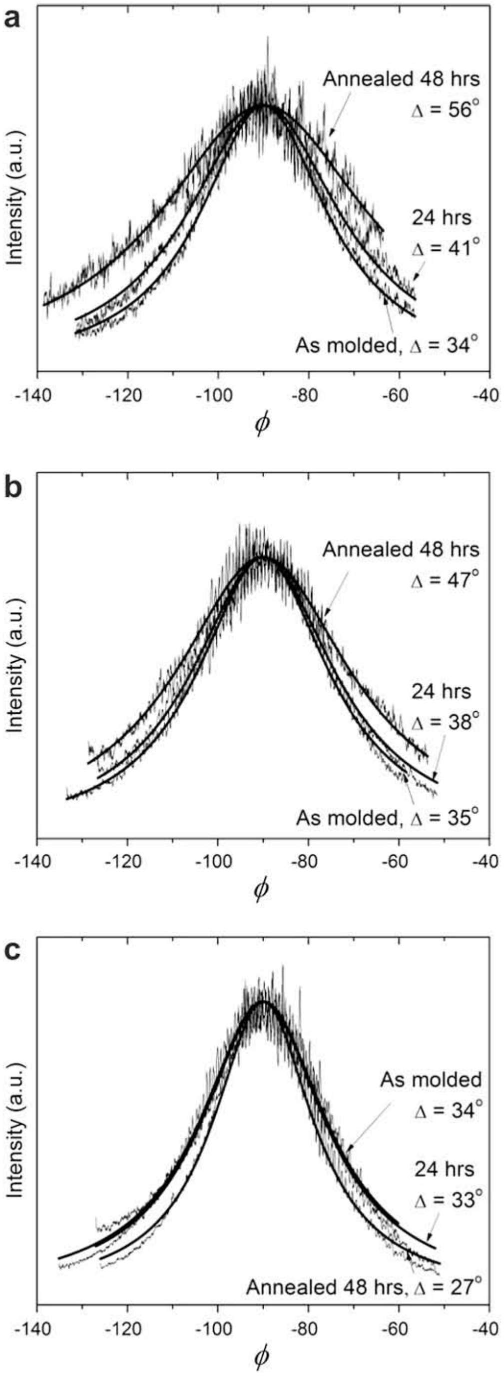

Fig. 5. Azimuthal X-ray scattering scans (scattered curves) at $2\theta = 26.4^\circ \pm 0.4$ in the flow direction and Lorentzian fits (smooth curves) using equation (1) for (a) 3 wt%, (b) 7 wt% and (c) 12 wt% graphite/PC D samples with varying annealing time: 0, 24 and 48 h. For clarity, scattering intensities were scaled to give the same peak heights.

X-ray scattering experiments were also performed on as-molded and annealed graphite D samples with varying annealing times. Fig. 5 shows the azimuthal scattering intensity profiles at $2\theta = 26.4^\circ$, with X-ray along the flow direction, of 3, 7 and 12 wt% graphite/PC disks annealed at 230 °C for 0, 24 and 48 h. The as-molded samples all exhibit intensity maxima around $\phi = -90^\circ$ indicating an anisotropic orientation of graphite. Spread in scattering intensity could be also quantified as the FWHM evaluated using equation (1). Quantified intensity spreads for as-molded disks are all around $\Delta = 33$–35° regardless of graphite concentration. In the case of 3 wt% graphite samples, this intensity concentration diminishes as annealing proceeds presumably due to particle disorientation. FWHM is relatively small before annealing, $\Delta = 34^\circ$ and grows to $\Delta = 41^\circ$ and 56° for samples annealed for 24 and 48 h, respectively. However, even after 48 h annealing, graphite orientation was not relaxed to the completely isotropic state indicating very slow disorientation processes. Although slower, the 7 wt% sample also displays a similar spread in scattering intensity over time: FWHM increases from 35° (as-molded) to 38° (24 h annealing) and 47° (48 h). However, the intensity scan of the 12 wt% sample barely changed with annealing. The FWHM turned out to be even smaller (33° and 27° for 24 and 48 h samples) than the un-annealed one (34°). This lack of disorientation processes in the 12 wt% sample can be explained by steric hindrance imposed by neighboring particles. Anisotropic inclusions such as rod-like or disk-like hard particles are known to form an ordered phase as the degree of anisotropy and volume fraction of particles increase [41,42]. Orientational freedom of these high aspect ratio platelets can be limited due to the volume excluded by particles in proximity. This is similar to the transition of discotic liquid crystals into the nematic phase. If, in fact, the 12 wt% graphite is in a nematic phase, an isotropic distribution will not be achieved even after prolonged annealing.

3.3. Melt rheology

Linear viscoelastic properties of graphite/PC and FGS/PC composite melts were studied with shear rheometry. Fig. 6 shows dynamic time sweeps of (a) graphite and (b) FGS composites. A time sweep for neat PC suggests a long-term thermal stability of PC melts. G' and G'' of PC changed less than 5% over 30,000 s. Matrix M_n ($\sim$27.3) and M_w ($\sim$50.5 kg/mol) measured after the time sweeps were identical with those of as-received and as-extruded Calibre 201-22. However, graphite or FGS composites behaved differently depending on the amount of the reinforcement added. G' of PC containing 1 and 3 wt% of graphite remained nearly unchanged over 8000–11,000 s (Fig. 6(a)). When graphite concentration was greater than 3 wt%, G' rose steadily over time. At longer time scale ($t > 7500$ s), logarithm of elastic modulus of 5, 7, 10 and 12 wt% samples grows almost linearly with logarithm of time, implying a power-law scaling ($G' \propto t^\beta$). The power-law exponent β evaluated at $t = 7500$–$10{,}000$ s was highest for the 7 wt% sample. A similar trend was observed for FGS samples (Fig. 6(b)): G' of the sample with intermediate FGS concentration, 1.5 wt% increased faster than that of 1.0 and 2.5 wt% as suggested by the highest exponent determined at $t = 15{,}000$–$20{,}000$ s. It should be also noted that G' increase of 1.0, 1.5 and 2.5 wt% FGS samples is slower than that of 5, 7 and 10 wt% graphite samples.

This G' increase with annealing time can be explained by the increased effective volume of rotating disks [43] and the restoration of an elastic network [44] which was disturbed by the squeezing

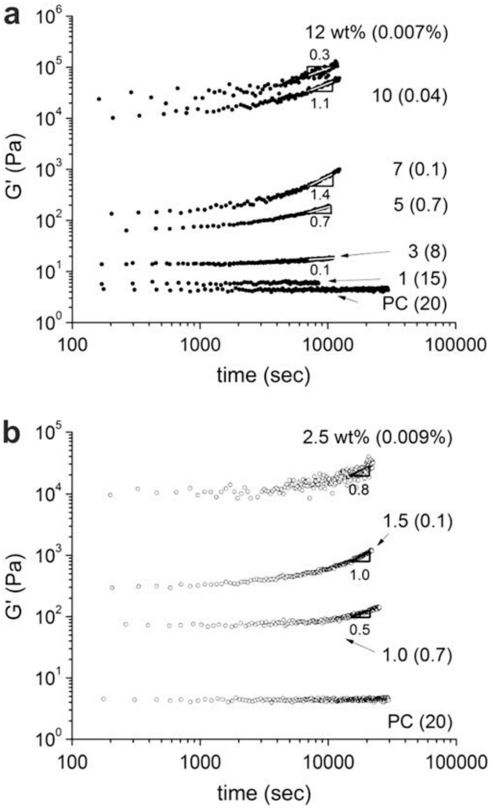

Fig. 6. Dynamic time sweeps at 0.1 rad/s of (a) graphite/PC and (b) FGS/PC composites at 230 °C. Scaling exponents shown were evaluated at $t = 7500–10{,}000$ s for graphite/PC and $t = 15{,}000–20{,}000$ s for FGS/PC composites. Values in parenthesis refer % test shear strains.

flow during sample loading. X-ray diffraction (Fig. 5) showed that particles start to disorient after the cessation of the flow and that disorientation of particles depends on particle concentration [45]. As illustrated in Fig. 7(a), even complete randomization of particles at very dilute concentration will not result in particle contact since their spheres of rotation will not intersect. This can explain the weak or no increase in G' for PC melts with low graphite or FGS concentration: the number density of particles is not high enough to form a percolated network. When the particle concentration becomes greater (Fig. 7(b)), platelets can interact after the rotary relaxation via direct contacts or bridging by polymer chains, and build a sample spanning filler network, which gives rise to the elastic response to small amplitude shearing. However, in the concentrated regime, isotropic orientation cannot be achieved due to excluded volume interactions between particles. This is illustrated by the fact that platelets in 12 wt% graphite samples remained correlated even after 48 h annealing (Figs. 5(c) and 7(c)). Due to this confinement, G' rise of the 12 wt% sample is significantly slower than that of 5 and 7 wt%.

After this structure recovery by long-term annealing, dynamic strain sweeps were carried out. Fig. 8 summarizes results from strain sweeps at 1 rad/s of (a) graphite and (b) FGS composites. This behavior is similar to flocculated gels [46–48]. Both graphite and FGS composites exhibit enhanced melt elasticity with increasing filler loading. They yield at large deformation, as characterized by a decline in G' with increased strain from the critical strain values. Critical strain γ_{crit} decreases at higher amount of graphite or FGS, which indicates formation of more fragile filler networks. The decrease in yield strain becomes more pronounced from a certain volume fraction of inclusions: between 3 and 5 wt% for graphite and between 1.0 and 1.5 wt% for FGS. These volume fractions coincide with the onset concentrations where the marked increase in G' during the time sweep starts to be monitored, implying they stem from a common origin: percolation of graphite network.

Dynamic frequency sweeps of PC composites after another annealing period of 10,000–12,000 s are shown in Fig. 9(a) and (c). G' at low frequency becomes independent of the test frequency above a critical concentration, which is a typical solid-like response of layered nanocomposite melts [7,22,49–51] and indicates formation of a network of filler–filler contacts. The transition from terminal to non-terminal behavior occurs between 3 and 5 wt% for graphite and between 1.0 and 1.5 wt% for FGS. These critical volume fractions agree with the onset of rigidity percolation found with time and strain sweeps (Figs. 6 and 8). From the percolation threshold ϕ_{per}, the particle average aspect ratio, A_f which is a ratio of diameter $2r$ to thickness h can be estimated assuming mono-dispersed disk-shaped particulates [7,50,52]:

$$A_f = \frac{2r}{h} = \frac{3\phi_{sphere}}{2\phi_{per}} \tag{2}$$

where $\phi_{sphere} = 0.29$, onset of percolation of interpenetrating, randomly packed spheres [53]. Using this formula with $\phi_{per,\ graphite} = 0.020$ (4 wt%) and $\phi_{per,\ FGS} = 0.006$ (1.25 wt%) gives $A_f \sim 22$ for graphite and ~ 72 for FGS. When converting the weight fraction to the volume fraction, densities of melt PC and graphite provided in Experimental Section were used. The higher aspect ratio of FGS agrees with the TEM results.

After loading and before each strain sweep and frequency sweep test, graphite and FGS were allowed to disorient for at least 10,000 s. However, Fig. 6 indicates that network growth is incomplete as G' of PC composites continuously rises. Rheological measurements were repeated after extended annealing ($t \sim 20{,}000$ s) for samples near or above the rigidity percolation: 5, 6 and 7 wt% graphite and 1.0, 1.5 and 2.0 wt% FGS composites (Fig. 9(b) and (d)). G' is higher for all samples, especially at low frequency, implying the elasticity kept growing during the additional 10,000 s of annealing. The rheological behavior of 1.0 wt% FGS sample was altered most dramatically from terminal (Fig. 9(c)) to frequency-independent (Fig. 9(d)). It suggests the FGS network can expand to the entire sample volume even at 1.0 wt%. Percolation volume fraction of 1.0 wt% corresponds to the average A_f of 90 according to equation (2). A_f values for graphite and FGS from melt rheology are compared with ones from other composite property measurements in Table 1.

Viscoelastic properties of polymer melts filled with anisotropic nano-particles can be greatly affected by flow [20,22,25]. Large strain shear or extensional flow may induce orientation of particles, and consequently a decrease in viscosity, storage and loss moduli of the suspension. A sequence of rheological tests on 0.5 wt% FGS/PC melts demonstrates dramatic changes in rheological responses depending on preceding flow history (Fig. 10). A time sweep test was first conducted on 0.5 wt% FGS/PC. G' rose steadily over 40,000 s (1-DTS) and eventually appeared to level off in the semi-logarithmic (log G' – linear time) plot. A frequency sweep (2-DFS) following 1-DTS indicated the presence of elastic FGS networks as evidenced by G' independent of frequency for $\omega < 0.1$ rad/s. A significant drop in elasticity at large amplitude strain (>1%) destroyed the fragile filler network (3-DSS). A series of strain sweeps (4,5 and 6-DSS) up to higher strain was used to completely orient the FGS layers. Orientation of FGS was confirmed with a frequency sweep (7-DFS) which showed the terminal response down to 0.2 rad/s. Then, the sample was annealed for another 40,000 s (8-DTS in Fig. 10(a)). 8-DTS and 9-DFS show re-formation of a viscoelastic solid. Rheological measurements demonstrate that these layered nanocomposite melts can undergo reversible changes

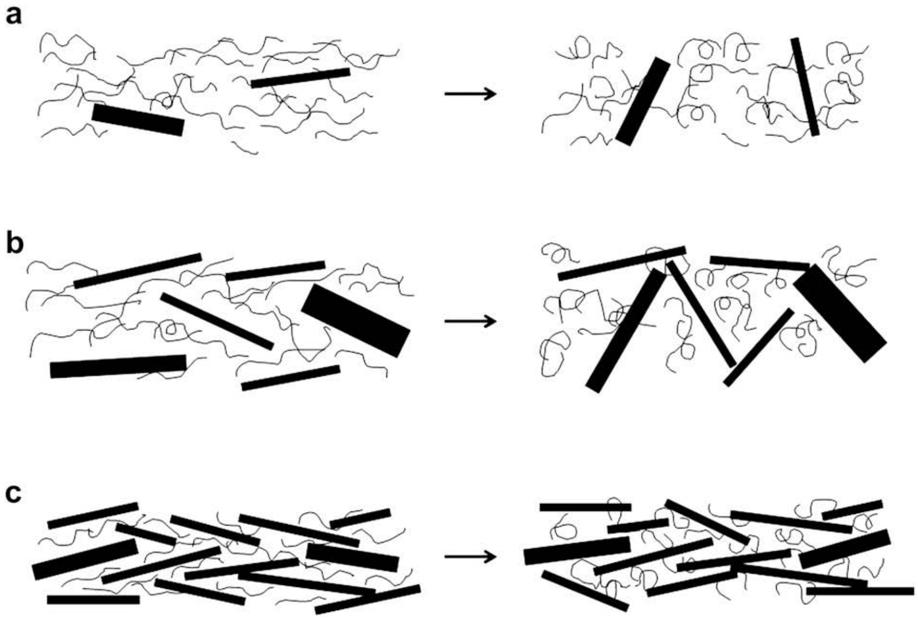

Fig. 7. Disorientation mechanisms for graphite at (a) dilute, (b) semi-dilute and (c) concentrated regime.

between liquid-like and solid-like state influenced by the previous history, e.g. large amplitude deformation and long-term annealing.

3.4. Mechanisms for particle disorientation

Randomization of nano-scale hard disks can be governed by either Brownian motions of particles [45], or other non-Brownian interactions [49,54–56]. Rotary diffusivity D_r of a circular Brownian disk with a diameter d in a medium with a viscosity η at temperature T is [45,55]

$$D_r = \frac{3kT}{4\eta d^3} \tag{3}$$

Assuming a rigid disk with average diameter, 200 nm [7], its rotary diffusion coefficient in PC at 230 °C ($\eta_0^* = 4000$ Pa s) is 1.6×10^{-4} s^{-1}. The rotational relaxation time $1/D_r = 60{,}000$ s is on the order of the experimental time for FGS network formation (40,000–50,000 s) in the semi-dilute condition (0.5 wt%, Fig. 10(a)). In the case of layered silicate/polymer composites, particle reorganization takes place much faster via particle–particle [49] or particle–matrix [54,56] interactions than expected by Brownian dynamics. Ren and coworkers [55] reported that growth in G' of layered silicates in polystyrene melts displays a logarithmic scaling on time ($G' \propto t^{\beta}$) under low amplitude oscillatory shearing, which is similar to the aging kinetics of soft colloidal glasses after quenching below the glass transition [57]. They also found that the particle randomization lacked Brownian characters (i.e. dependence on temperature and matrix viscosity). In fact, modulus of PC composite melts also follows this scaling at $t > 10{,}000$ s signifying its analogy to aging colloidal glasses (Figs. 6 and 10 (a) inset). Moreover, although particle disorientation was not detected from X-ray scattering for the 12 wt% graphite/PC melt, G' rose steadily implying the elasticity gain cannot simply be correlated with rotary relaxation of disks. Abou and coworkers [58] found that in aqueous suspensions of Laponite, an average relaxation time required for the escape of particles from "cages" formed by their neighbors via Brownian motions increases exponentially with the aging time. Likewise, as the system ages, the "cage diffusion" of graphitic particles will become more difficult, thus raising the viscoelasticity of the suspension.

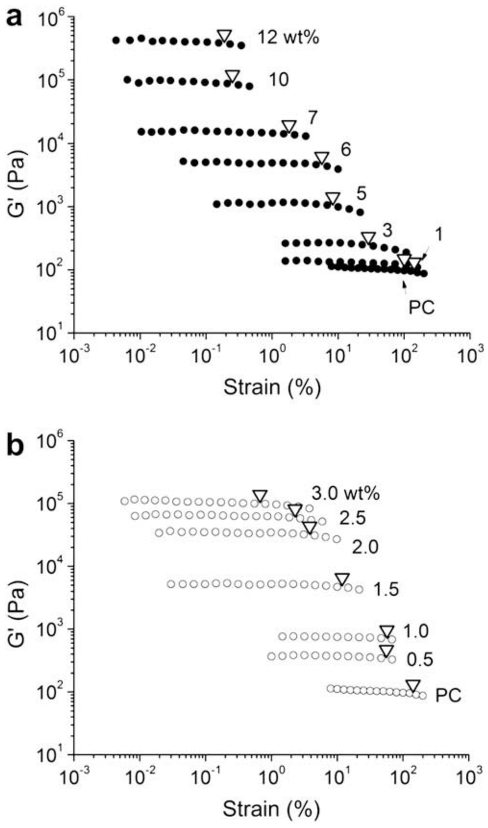

Fig. 8. Dynamic strain sweeps at 1 rad/s of (a) graphite and (b) FGS/PC composites at 230 °C. Critical strains by the 90% rule are marked with ∇.

3.5. Electrical conductivity

The DC surface resistance of FGS/PC and graphite/PC composites with three different geometries (D, F and B samples) is tabulated in Tables 2 and 3. Fig. 11 shows how different types of graphite

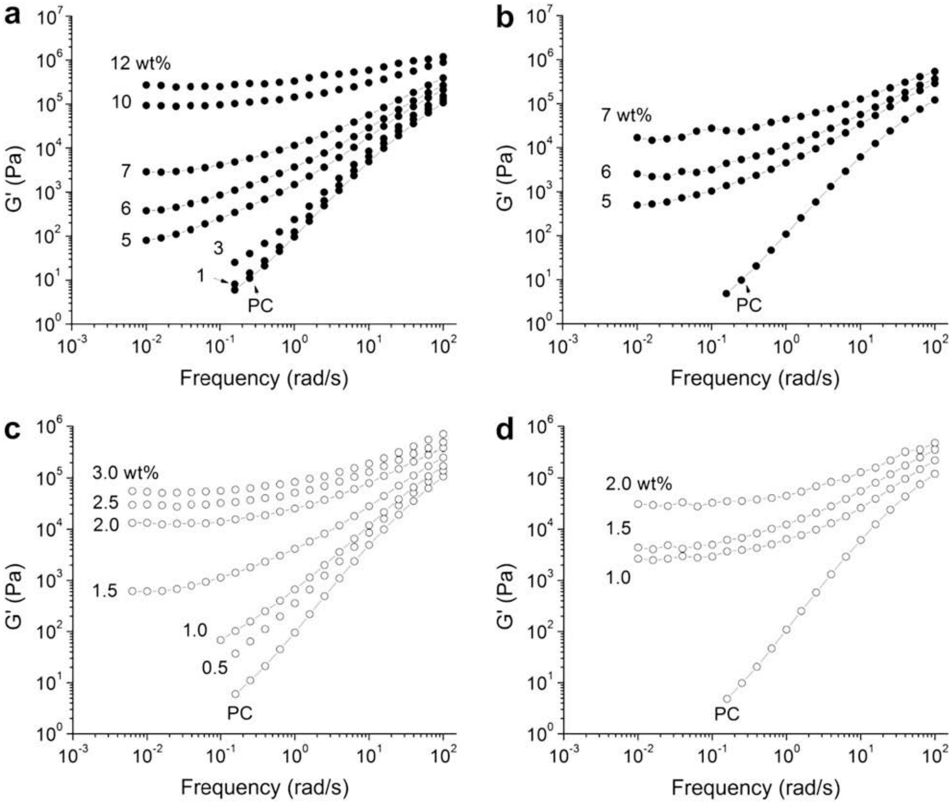

Fig. 9. Dynamic frequency sweeps of graphite/PC melts after annealing for (a) 10,000 and (b) 20,000 s, and FGS/PC melts after annealing for (c) 10,000 and (d) 20,000 s at 230 °C.

additives and processing influence the surface resistance of PC. While both graphite and FGS improve the electrical conductivity of PC implying electrical percolation within the matrix, the resistance of FGS composites begins to decrease at much lower concentration.

As well as the state of dispersion, orientation of nano-fillers is also important for determining electrical conduction of composites [24]. We can see this by comparing electrical percolation and graphite orientation quantified with X-ray scattering of D and F samples. Threshold volume fraction ϕ_{per} of graphite and FGS for electrical percolation was determined as the concentration of composites where their resistance decreases to 10% of the resistance of neat PC. These are summarized in Table 1 along with rheological percolation. The corresponding A_f values calculated using equation (2) are also shown. For both graphite and FGS composites, ϕ_{per} of F samples is substantially greater than that of D samples implying that flow during compression molding aligns the disk-like particles, losing connectivity between them. Percolation thresholds and A_f of D samples from conductivity and rheological measurements are in good agreement. As azimuthal X-ray scattering scans suggest (Figs. 4 and 5), graphite orientation in the annealed D samples is less pronounced than that in F samples. Therefore, electrical percolation of D samples better describes the level of dispersion since equation (2) assumes a perfectly random orientation of disks.

Note that resistance of the 10 wt% graphite B sample measured on the unpolished surface is significantly higher than for the polished surface (see the inset in Fig. 11). A thin skin layer of PC formed during injection molding probably interfered with the conductivity measurements; removing ~10 μm thick skin exposed graphite particles to the surface.

3.6. Mechanical properties

Another benefit from graphite dispersion is that it can improve stiffness and dimensional stability of polymers substantially by small incorporation of nano-platelets with high aspect ratio and excellent in-plane mechanical properties [1,2,6,7,59]. Stiffness and thermal expansion of graphite/PC and FGS/PC composites were measured from dynamic mechanical analysis with RSA II and presented with other solid composite properties in Tables 2 and 3.

Table 1
Percolation volume fraction and aspect ratio of graphite and FGS.

Sample	Electrical conductivity		Melt rheology		Tensile modulus	Thermal expansion	N_2 permeation
	ϕ_{per}	A_f	ϕ_{per}	A_f	A_f	A_f	A_f
Graphite, D[a]	0.027–0.033	15	0.015–0.025	20	–	–	–
Graphite, F	0.047–0.055	9	–	–	19	19	11
FGS, D[a]	0.005–0.007	73	~0.005	90	–	–	–
FGS, F	0.008–0.011	46	–	–	21[b]	30[b]	51

[a] Note that the electrical percolation is from solid D samples annealed for 48 h and the rheological percolation is from frequency sweeps of melt samples following time sweeps for 20,000 s (Fig. 9(b) and (d)).

[b] Note that these aspect ratio values were obtained using in-plane tensile modulus and CTE of graphite.

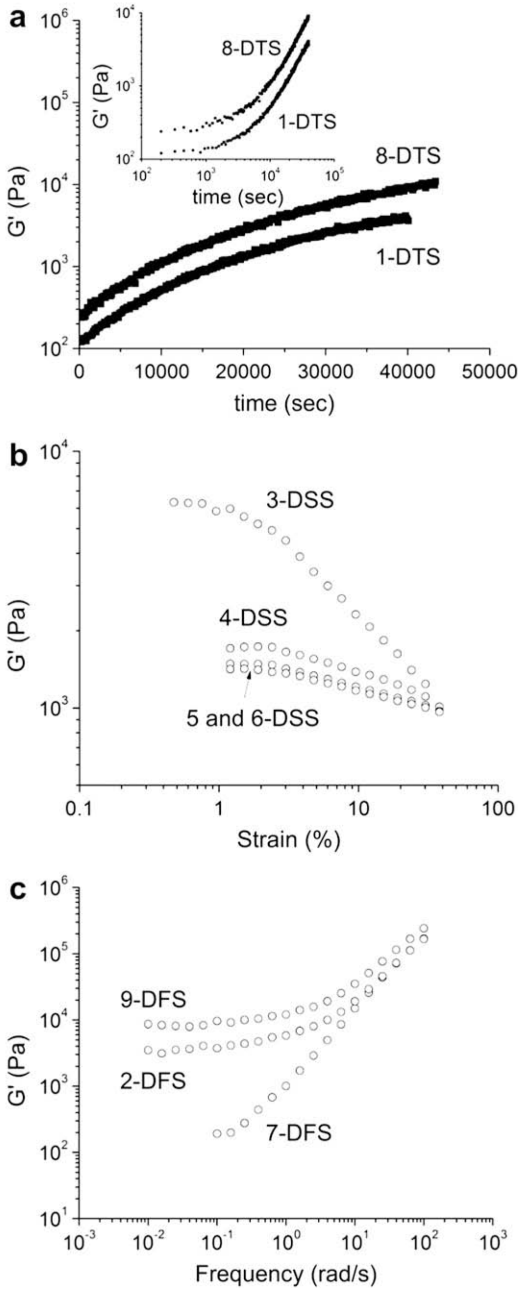

Fig. 10. In the sequence 1–9, a single sample of 0.5 wt% FGS/PC was subjected to (a) dynamic time sweeps at 0.1 rad/s, (b) strain sweeps at 1 rad/s and (c) frequency sweeps at 230 °C. (a) The inset shows time sweep results in a double-logarithmic plot.

3.6.1. *Tensile and blending modulus*

Fig. 12 shows dynamic tensile and 3-point bending moduli of graphite composites and tensile moduli of FGS composites normalized by modulus of neat PC. Addition of either graphite or FGS increases the stiffness of PC. Young's modulus of 15 wt% graphite composites is ~150% higher than modulus of neat polymer (2.1 GPa). There is also a notable increase in bending stiffness of PC. Bending modulus of PC (2.6 GPa) was improved by ~60% by incorporating 10 wt% of graphite, which is a slightly less enhancement than that in tensile modulus (~80%) that same amount of graphite can offer. However, despite its higher aspect ratio, modulus gains by FGS are not significantly higher than ones by graphite. E of 2 wt% FGS composites (2.51 GPa) is slightly higher than that of 3 wt% graphite composites (2.45 GPa). Substantially greater modulus increase (~80%) by only 1 wt% of FGS was reported for poly(methyl methacrylate) (PMMA, $E = 2.1$ GPa) by Ramanathan and coworkers [60]. However, their composites were produced via solvent processing which generally leads to better dispersion than melt compounding. Also, the pendant carbonyl groups on PMMA are expected to have stronger interactions with polar oxygens on FGS surface.

Stiffness of composites reinforced with ellipsoidal inclusions can be predicted by a micromechanical model proposed by Mori and Tanaka [61]. Tandon and Weng adapted Mori and Tanaka's model to derive analytical forms for effective transverse modulus E_{11} of composites with unidirectionally aligned, mono-dispersed ellipsoids [62].

$$\frac{E_{11}}{E_m} = \frac{1}{1+\phi(-2\nu_m A_3+(1-\nu_m)A_4+(1+\nu_m)A_5A)/2A} \tag{4}$$

where φ, E_m and ν_m are concentration of the filler, Young's modulus and Poisson's ratio of the matrix. Formulas for A and A_i which are functions of φ, ν_m and components of Eshelby's tensor [63,64] are provided in Tandon and Weng. Assuming graphite and FGS particles incorporated in PC can be approximated by ellipsoids, their average aspect ratio was estimated with matrix ($E_{PC} = 2.1$ GPa) and in-plane filler modulus ($E_{graphite} = 1060$ GPa) [4,34], matrix ($\nu_{PC} = 0.37$) [65] and filler Poisson's ratio ($\nu_{graphite} = 0.006$) [66] which are required to compute A and A_i. The aspect ratio of graphite is 19, which is close to A_f from melt rheology and electrical conductivity measurements (Table 1). Although Poisson's ratio of graphite are reported in a wide range ($\nu_{graphite} = -0.171$–4.958) [66], the result was not changed appreciably ($A_f = 19$–20) by using different reported $\nu_{graphite}$ due to small thickness of graphite. Note that the trend for bending stiffness of graphite composites shown in Fig. 12(a) is a linear fit, not based on the Mori–Tanaka theory. The average A_f of FGS from composite modeling is 21 which is far smaller than ones inferred via other characterization routes.

We previously reported this same low stiffening performance of FGS for poly(ethylene-2,6-naphthalate) and explained it by differences between graphite and FGS structure [7]. In Fig. 2(f), FGS appears to have an accordion-like structure composed of irregularly wrinkled sheets. FGS is formed by oxidation and superheating of graphite which may result in significant structural distortions such as sheet crumpling and atomistic vacancies [17]. Stiffening performance of graphene layers could be reduced by these processes since their main deformation mode under in-plane tensile stress will be straightening of wrinkled sheets rather than stretching of, or bending between C–C bonds, which accounts for the extremely high stiffness of planar graphene. Moreover, the high diameter to thickness ratio of FGS will render it more flexible than graphite. Graphene thin films, often called 2-dimensional macromolecules [67] can be frozen into a curved structure within the polymer matrix, which further reduces their effective stiffening efficiency. Schniepp et al. also found that folding of the sheets can be aided by pre-existing defect lines on FGS [68]. It should be also noted that Tandon and Weng assumed unidirectional alignments of mono-dispersed ellipsoids with perfect matrix adhesion, which is hardly realized in practice. Fig. 4(b) suggests that graphite orientation even in compression molded F samples is far from perfect in-plane orientation ($\Delta = 0°$). Deviation from the complete planar orientation can reduce composite modulus substantially [69]. Modulus estimation for PC composites containing 10 wt% ($\phi = 0.055$) of graphite platelets ($A_f = 20$) based on equation (13) in reference [69] and

Table 2
Solid properties of PC/graphite composites.

Concentration		Surface resistance			Gas permeability		Modulus		CTE
					He	N_2	Tensile	Bending	
wt%	vol%	*F*(ohms)	*D*[a](ohms)	*B*(ohms)	*F*(Barrer)		*F(GPa)*	*B(GPa)*	*F* ($\times 10^5$/°C)
0	0	1.3×10^{13}	8.8×10^{13}	5.5×10^{13}	12.5	0.36	2.08	2.58	7.89
1	0.5	2.8×10^{13}	5.1×10^{13}	4.3×10^{13}	–	–	2.16	2.76	7.56
3	1.6	–	7.7×10^{13}	–	10.6	0.32	2.45	–	6.70
5	2.7	–	3.7×10^{13}	3.4×10^{13}	9.32	0.31	2.50	3.21	6.28
6	3.3	–	1.4×10^{12}	–	–	–	–	–	–
7	3.8	3.5×10^{13}	1.7×10^{9}	–	8.61	0.26	2.96	–	5.43
8.5	4.7	7.8×10^{12}	1.9×10^{7}	–	8.02	0.26	3.36	–	5.85
10	5.5	7.3×10^{11}	3.3×10^{6}	7.6×10^{7}	7.29	0.21	3.69	4.23	4.57
12	6.7	1.5×10^{10}	3.4×10^{5}	–	6.82	0.23	4.16	–	4.89
15	8.5	1.6×10^{7}	7.8×10^{4}	–	–	–	5.17	–	3.53

[a] Annealed for 48 h.

the Mori–Tanaka's theory suggests that tensile stiffness can vary from 3.26 for 3-dimensional random alignment to 3.84 Pa for unidirectional orientation.

3.6.2. *Thermal expansion*

Coefficients of thermal expansion (CTE) of PC composites evaluated from dynamic temperature sweeps are shown in Fig. 13. Substantial decrease in thermal expansion of PC is evident for both composites. This can be compared to Chow's micromechanical theory [70] which predicts transverse linear CTE, α_{11} of composites containing unidirectionally aligned mono-dispersed ellipsoidal dispersions

$$\alpha_{11} = \alpha_m + \frac{K_f}{K_m}\,\frac{\left(\beta_f - \beta_m\right)J_3\phi}{2I_1J_3 + J_1I_3} \tag{5}$$

where β_i and K_i are the volumetric thermal expansion coefficient and the bulk modulus of filler f or matrix m, respectively. I_j and J_j ($j = 1$ or 3) are functions [70] of β_i, K_i, shear moduli G_i of each component, volume fraction of filler ϕ and components of Eshelby's tensor [63,64]. For the calculation of β_i, K_i and G_i, refer to Appendix A in reference [7]. Assuming PC is isotropic, β_{PC} was estimated from experimentally measured linear CTE ($\alpha_{PC\parallel} = \alpha_{PC\perp} = 7.9 \times 10^{-5}$/°C). For graphite and FGS, $\alpha_{\parallel} = -1.5 \times 10^{-6}$ and $\alpha_{\perp} = 27 \times 10^{-6}$/°C [71,72]. Fitting the experimental data with Chow's model gives an average A_f of FGS (30), slightly higher than that of graphite ($A_f = 19$). While graphite shows a good agreement in A_f estimated from other techniques (Table 1), FGS turns out to be only marginally better than graphite in reducing thermal expansion of PC considering its high A_f. Again, we believe that the structural distortion and higher flexibility of FGS increase its effective thermal expansion.

3.7. *Gas barrier properties*

Permeation rate of gas molecules diffusing through membranes can be decreased by embedding high aspect ratio, impermeable particles that provide tortuous paths and reduce the cross sectional area available for permeation [73]. Graphite can be a good candidate for these types of reinforcements due to its high aspect ratio [6–8]. N_2 and He permeation through PC films (F samples) reinforced with graphite and FGS were evaluated at 35 °C (Fig. 14). Permeability of neat PC is in close agreement with reported values ($P_{He} = 13.6$, $P_{N_2} = 0.29$ Barrers at 35 °C) [74]. While both additives are capable of suppressing N_2 and He permeation, the permeability of FGS composites is significantly smaller than that of graphite composites. Composite modeling can be also performed to quantitatively estimate A_f from gas permeation data of composites [7,75]. Lape and co-workers' model for membranes dispersed with impermeable anisotropic flakes in a random array gives [76]

$$\frac{P}{P_m} = \frac{1-\phi}{\left(1 + A_f\phi/3\right)^2} \tag{6}$$

where P_m and P are gas permeabilities through unfilled and filled membranes and ϕ is the volume fraction of added particles. Equation (6) predicts that graphite decreases gas permeation as much as impermeable flakes with $A_f = 11$–14, while for FGS $A_f = 51$ for N_2 permeation and 39 for He. Better dispersion for FGS is in line with observation from the other methods. However, the values of A_f for FGS (39–51) are lower than the values from melt rheology and electrical conductivity measurements (Table 1). Equation (6) assumes that embedded disks have perfect planar alignment. From the X-ray scattering results (Fig. 4(b)), some misalignment of

Table 3
Solid properties of PC/FGS composites.

Concentration		Surface resistance		Gas permeability		Tensile modulus	CTE
				He	N_2		
wt%	vol%	*F* (ohms)	*D*[a](ohms)	*F* (Barrer)		*F* (GPa)	*F* ($\times 10^5$/°C)
0	0	1.3×10^{13}	8.8×10^{13}	12.5	0.36	2.08	7.89
0.25	0.13	–	1.8×10^{13}	–	–	–	–
0.50	0.26	7.2×10^{12}	2.4×10^{13}	11.5	0.33	2.15	7.17
0.75	0.40	–	1.9×10^{13}	–	–	–	–
1.00	0.53	9.8×10^{12}	2.4×10^{13}	–	–	2.22	7.07
1.25	0.66	–	3.3×10^{8}	–	–	–	–
1.50	0.80	7.3×10^{12}	1.6×10^{6}	10.2	0.30	2.27	7.11
2.00	1.06	1.1×10^{8}	8.0×10^{5}	9.7	–	2.51	6.64
2.50	1.33	6.4×10^{6}	6.6×10^{5}	8.9	0.24	2.51	6.73
3.00	1.60	2.8×10^{6}	2.0×10^{5}	8.8	0.20	–	–

[a] Annealed for 48 h.

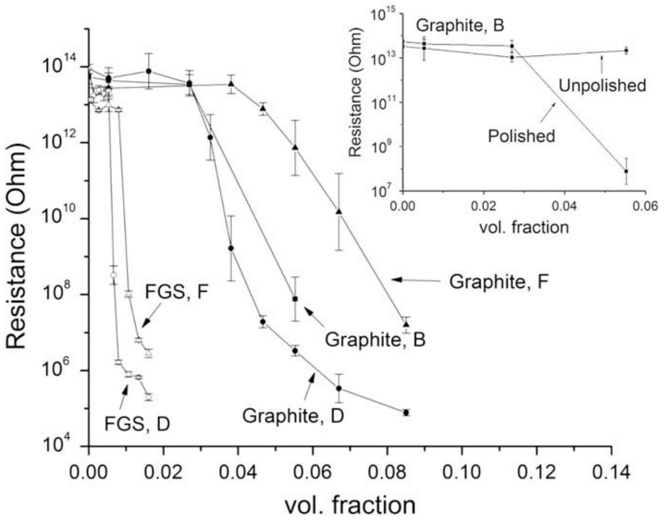

Fig. 11. Surface resistance of graphite and FGS/PC composites. D: denoted by circles. ~1 mm thick disks annealed for 48 h at 240 °C. F: triangles. ~150 μm thick films from compression molding at 260 °C. B: rectangles. 10 cm × 3.25 mm × 12.8 mm injection molded bars. The inset compares resistance values measured on the polished surface and the unpolished surface of graphite B samples.

graphite can be inferred, which potentially reduces the barrier efficiency of the composites [19]. For instance, the relative permeability (P/P_m) of PC filled with 3 wt% ($\phi = 0.016$) graphene layers ($A_f = 90$) can vary between 0.57 (perfect planar alignment) and 0.79 (random orientation) based on equation (4) in reference [19]. Interestingly, FGS appears to be slightly better for blocking diffusion of N_2 than He as the higher A_f from N_2 diffusion measurements suggests. On the FGS surfaces, there can be atomistic perforations that CO_2 evolution left during pyrolysis treatments, which more likely allow penetration of smaller molecules such as He than larger ones: the kinetic diameter of N_2 is 3.64 Å versus 2.89 Å for He [77]. Furthermore, increased free volume near the graphene-PC interface may selectively expedite transmission of smaller permeants [78].

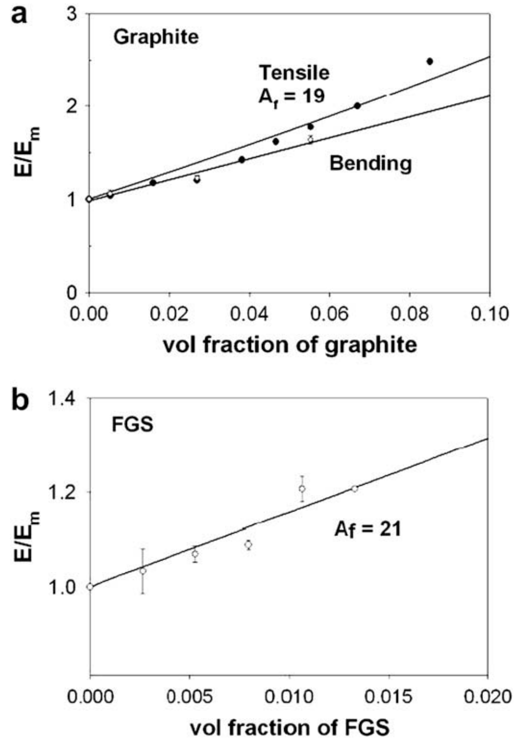

Fig. 12. (a) Tensile (denoted by closed circles) and bending (open circles with error bars) modulus of graphite/PC composites normalized by stiffness of neat PC. A trend for tensile modulus based on the Mori–Tanaka theory and a linear fit of bending modulus data are also shown. (b) Tensile modulus of FGS/PC composites with a fit based on the Mori–Tanaka model as A_f an adjustable parameter.

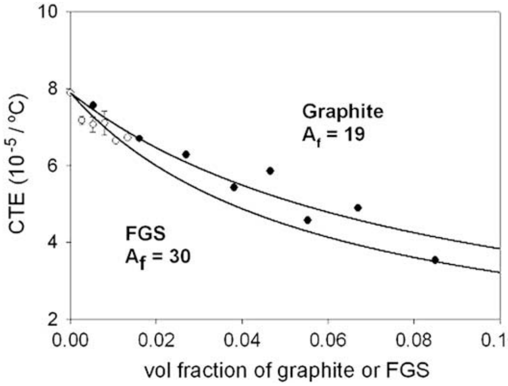

Fig. 13. Coefficients of thermal expansion of graphite (closed) and FGS (open symbols) composites. Solid curves represent model predictions based on Chow's theory.

4. Summary

Graphite and thermally exfoliated graphite oxide (FGS) were blended into PC via melt extrusion. Electron microscopy and X-ray diffraction revealed un-intercalated morphology of graphite, while FGS appears to be highly exfoliated throughout the entire matrix. From 2-dimensional X-ray diffraction, flow induced orientation of graphite in compression or injection molded samples was also confirmed. While graphite orientation in dilute conditions can be relaxed toward an isotropic state by thermal annealing, particles at

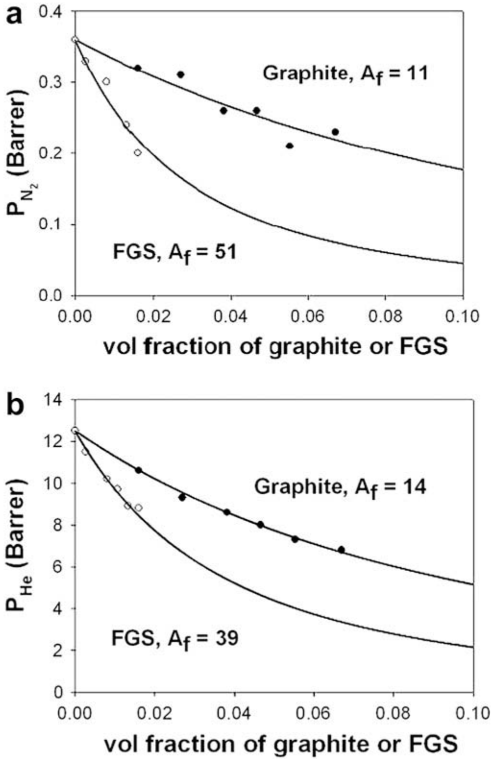

Fig. 14. (a) N_2 and (b) He permeation constants of graphite and FGS/PC composites at 35 °C. Curves are predictions based on the model of Lape and coworkers.

high concentration remain aligned even after prolonged annealing due to geometric restrictions.

Melt rheology was employed to investigate viscoelastic properties of the PC composites. After annealing for 10,000 s, both graphite and FGS in PC exhibit solid-like responses above rigidity percolation, which is between 3 and 5 wt% for graphite and 1.0 and 1.5 wt% for FGS. However, with extended annealing, even 0.5 wt% FGS composites become viscoelastic solids. Percolation concentration of 0.5 wt% is considerably lower than that of melt-mixed expanded graphite (~4 wt%) [51] or multi-walled carbon nanotubes (1–2 wt%) [26,27] in the same polymer. The 0.5 wt% FGS sample also shows interesting reversibility between liquid-like and solid-like behavior, affected by previous processing: long-term annealing and large amplitude shearing.

Surface resistance of PC composites starts to drop precipitously above connectivity percolation concentrations (6 wt% for graphite and 1.25 wt% for FGS) which are in agreement with the rigidity percolation from melt rheology. At the same filler concentration, electrical conductivity of squeezed films or injection molded samples is noticeably lower than annealed disks, which is attributed to alignment of graphitic platelets.

Both graphite and FGS lead to improved PC stiffness and dimensional stability. However, the increase in modulus and the decrease in CTE from FGS dispersion are not as significant as expected from the high aspect ratio found via percolation. Sheet wrinkling and atomistic defects on the surface after oxidation and pyrolysis treatments may account for its low performance in mechanical properties. N_2 and He permeability could be reduced by incorporation of graphite and FGS. Interestingly, FGS turns out to be more effective barrier against diffusing molecules with a larger kinetic diameter implying its potential for materials for gas separation.

We found a dramatic variation in composite properties which is influenced by both dispersion and orientation of graphitic reinforcements. In order to achieve highest property enhancements, morphology of polymer/graphite composites must be controlled properly. Even though higher aspect ratio of additives is favorable for most applications, high flexibility of thin sheets may reduce their stiffening performance. In applications that require good melt viscoelasticity and electrical conductivity, isotropic filler orientation is desired. However, most conventional manufacturing processes such as injection molding and extrusion will orient graphite particles, which may improve stiffness and barrier properties in specific directions but also reduce electrical conductivity gains.

Acknowledgements

The authors acknowledge research grants from General Motors Corp. and the University of Minnesota Industrial Partnership for Research in Industrial and Materials Engineering (IPRIME). We would like to thank John Lettow of Vorbeck Materials for providing the FGS, Adam Reimnitz for help with melt processing and property measurements, Prof. Michael Tsapatsis at the University of Minnesota for use of the gas permeation apparatus, Mingjun Yuan at Entegris for use of electrical conductivity measurements. Parts of this work were carried out in the University of Minnesota I.T. Characterization Facility, which receives partial support from NSF through the NNIN program and in the Polymer Characterization Facility, which receives partial support from the NSF funded University of Minnesota MRSEC.

References

[1] Drzal LT, Fukushima H. Polym Prepr (Am Chem Soc Div Polym Chem) 2001;42:42.
[2] Fukushima H, Drzal LT. Ann Tech Conf Soc Plast Eng 2003:2230.
[3] Blakslee OL, Proctor DG, Seldin EJ, Spence GB. J Appl Phys 1970;41:3373.
[4] Lee C, Wei X, Kysar JW, Hone J. Science 2008;321:385.
[5] Tsuzuku T. Carbon 1979;17:293.
[6] Kalaitzidou K, Fukushima H, Drzal LT. Carbon 2007;45:1446.
[7] Kim H, Macosko CW. Macromolecules 2008;41:3317.
[8] Prud'homme RK, O'Neil CD, Ozbas B, Aksay IA, Register RA, Adamson DH. 2007; WO 2008130431.
[9] Carr KE. Carbon 1970;8:155.
[10] Zheng W, Wong S-C, Sue H-J. Polymer 2002;43:6767.
[11] Zou J-F, Yu Z-Z, Pan Y-X, Fang X-P, Ou Y-C. J Polym Sci Part B Polym Phys 2002;40:954.
[12] Fukushima H. PhD Thesis. Michigan State University; 2003.
[13] Al-Jishi R, Dresselhaus G. Phys Rev B 1982;26:4514.
[14] Schniepp HC, Li J-L, McAllister MJ, Sai H, Herrera-Alonso M, Adamson DH, et al. J Phys Chem B 2006;110:8535.
[15] Prud'homme RK, Aksay IA, Adamson DH, Abdala A. 2007; US Patent 20070092432 A1.
[16] McAllister MJ, Li J-L, Adamson DH, Schniepp HC, Abdala AA, Liu J, et al. Chem Mater 2007;19:4396.
[17] Li J-L, Kudin KN, McAllister MJ, Prud'homme RK, Aksay IA, Car R. Phys Rev Lett 2006;96:176101/1.
[18] Hull D, Clyne TW. An introduction to composite materials. 2nd ed. London: Cambridge University Press; 1996.
[19] Bharadwaj RK. Macromolecules 2001;34:9189.
[20] Du F, Scogna RC, Zhou W, Brand S, Fischer JE, Winey KI. Macromolecules 2004;37:9048.
[21] Celzard A, McRae E, Deleuze C, Dufort M, Furdin G, Mareche JF. Phys Rev B 1996;53:6209.
[22] Krishnamoorti R, Giannelis EP. Macromolecules 1997;30:4097.
[23] Balberg I, Binenbaum N. Phys Rev B 1983;28:3799.
[24] Du F, Fischer JE, Winey KI. Phys Rev B 2005;72:121404/1.
[25] Kharchenko SB, Douglas JF, Obrzut J, Grulke EA, Migler KB. Nat Mater 2004; 3:564.
[26] Potschke P, Fornes TD, Paul DR. Polymer 2002;43:3247.
[27] Potschke P, Dudkin SM, Alig I. Polymer 2003;44:5023.
[28] http://automotive.dow.com/materials/products/calibre/201.htm, [accessed 18.06.09].
[29] www.asbury.com, [accessed 18.06.09].
[30] Brunauer S, Emmett PH, Teller E. J Am Chem Soc 1938;60:309.
[31] Tamashuasky AV. Surface enhanced flake graphite and its utility as a functional extender for molybdenum disulfide. National Lubricating Grease Institute 72nd Annual Meeting, San Antonio, TX, 2005.
[32] www.vorbeck.com, [accessed 18.06.09].
[33] Bohlen J, Kirchheim R. Macromolecules 2001;34:4210.
[34] Kelly BT. Physics of graphite. 1st ed. London: Applied Science; 1981.
[35] Kudin KN, Ozbas B, Schniepp HC, Prud'homme RK, Aksay IA, Car R. Nano Lett 2008;8:36.
[36] Maric M, Macosko CW. Polym Eng Sci 2001;41:118.
[37] Spitael P, Macosko CW. Polym Eng Sci 2004;44:2090.
[38] Pye DG, Hoehn HH, Panar M. J Appl Polym Sci 1976;20:1921.
[39] Jeong H-K, Krych W, Ramanan H, Nair S, Marand E, Tsapatsis M. Chem Mater 2004;16:3838.
[40] Haggenmueller R, Gommans HH, Rinzler AG, Fischer JE, Winey KI. Chem Phys Lett 2000;330:219.
[41] Forsyth Jr PA, Marcelja S, Mitchell DJ, Ninham BW. Adv Colloid Interface Sci 1978;9:37.
[42] Davis VA, Ericson LM, Parra-Vasquez ANG, Fan H, Wang Y, Prieto V, et al. Macromolecules 2004;37:154.
[43] Bonn D, Kellay H, Tanaka H, Wegdam G, Meunier J. Langmuir 1999;15:7534.
[44] Alig I, Skipa T, Lellinger D, Poetschke P. Polymer 2008;49:3524.
[45] Larson RG. The structure and rheology of complex fluids. New York: Oxford Press; 1999.
[46] Mewis J, Spaull AJB. Adv Colloid Interface Sci 1976;6:173.
[47] Patel PD, Russel WB. J Rheol 1987;31:599.
[48] Rueb CJ, Zukoski CF. J Rheol 1997;41:197.
[49] Solomon MJ, Almusallam AS, Seefeldt KF, Somwangthanaroj A, Varadan P. Macromolecules 2001;34:1864.
[50] Vermant J, Ceccia S, Dolgovskij MK, Maffettone PL, Macosko CW. J Rheol 2007;51:429.
[51] Abdel-Goad M, Poetschke P, Zhou D, Mark JE, Heinrich G. J Macromol Sci Part A 2007;44:591.
[52] Ren J, Silva AS, Krishnamoorti R. Macromolecules 2000;33:3739.
[53] Shante VKS, Kirkpatrick S. Adv Phys 1971;20:325.
[54] Schmidt G, Nakatani AI, Butler PD, Karim A, Han CC. Macromolecules 2000;33:7219.
[55] Ren J, Casanueva BF, Mitchell CA, Krishnamoorti R. Macromolecules 2003;36:4188.
[56] Lele A, Mackley M, Galgali G, Ramesh C. J Rheol 2002;46:1091.
[57] Bonn D, Tanase S, Abou B, Tanaka H, Meunier J. Phys Rev Lett 2002;89:015701/1.
[58] Abou B, Bonn D, Meunier J. Phys Rev E 2001;64:021510/1.
[59] Kalaitzidou K, Fukushima H, Drzal LT. Composites Part A 2007;38:1675.
[60] Ramanathan T, Abdala AA, Stankovich S, Dikin DA, Herrera-Alonso M, Piner RD, et al. Nat Nanotechnol 2008;3:327.
[61] Mori T, Tanaka K. Acta Metall 1973;21:571.
[62] Tandon GP, Weng GJ. Polym Compos 1984;5:327.

[63] Eshelby JD. Proc Roy Soc (London) 1957;241:376.
[64] Eshelby JD. Proc Roy Soc (London) 1959;252:561.
[65] Gilmour IW, Trainor A, Haward RN. J Appl Polym Sci 1979;23:3129.
[66] Cho J, Luo JJ, Daniel IM. Compos Sci Technol 2007;67:2399.
[67] Wen X, Garland CW, Hwa T, Kardar M, Kokufuta E, Li Y, et al. Nature 1992;355:426.
[68] Schniepp HC, Kudin KN, Li J-L, Prud'homme RK, Car R, Saville DA, et al. ACS Nano 2008;2:2577.
[69] Fornes TD, Paul DR. Polymer 2003;44:4993.
[70] Chow TS. J Polym Sci Part B Polym Phys 1978;16:967.
[71] Nelson JB, Riley DP. Proc Phys Soc 1945;57:477.
[72] Kelly BT. Carbon 1972;10:429.
[73] Cussler EL, Hughes SE, Ward III WJ, Aris R. J Membr Sci 1988;38:161.
[74] Pixton MR, Paul DR. Relationship between structure and transport properties for polymers with aromatic backbones. In: Paul DR, Yampol'skii YP, editors. Polymeric gas separation membranes. Boca Raton: CRC Press; 1994. p. 83.
[75] Picard E, Vermogen A, Gerard JF, Espuche E. J Membr Sci 2007;292:133.
[76] Lape NK, Nuxoll EE, Cussler EL. J Membr Sci 2004;236:29.
[77] Cussler EL. Diffusion: mass transfer in fluid systems. 2nd ed. Cambridge: Cambridge University Press; 1997.
[78] Osman MA, Mittal V, Morbidelli M, Suter UW. Macromolecules 2003;36:9851.